Available online at www.sciencedirect.com
SCIENCE DIRECT®
PERGAMON
International Journal of Heat and Mass Transfer 46 (2003) 3029–3039
International Journal of HEAT and MASS TRANSFER
www.elsevier.com/locate/ijhmt

Heat and mass transfer of a convective-stratified flow in a trough type tundish

A. Vargas-Zamora, R.D. Morales *, M. Díaz-Cruz, J. Palafox-Ramos, L. García Demedices

Department of Metallurgy and Materials Engineering, Instituto Politécnico Nacional-ESIQIE, Apdo. Postal 75-874, México D.F. CP 07300, Mexico

Received 24 June 2002; received in revised form 27 December 2002

Abstract

Fluid flow, heat and mass transfer of liquid steel in a trough type tundish were physically and mathematically simulated using a water model. Flow structures were determined through particle image velocimetry (PIV) techniques. Under isothermal conditions fluid flow approaches that of a plug pattern. Non-isothermal conditions provoked long recirculating flows along the vessel and makes the flow to departure form the plug pattern. Buoyancy forces increased fluid velocities close to the bath surface and enhanced convection mass transfer of a tracer injected in the flow and the flotation of solid particles. Measured fluid velocity fields maintained an acceptable good agreement with mathematical simulations under isothermal and non-isothermal conditions.

Keywords: Mixed convection; Heat and mass transfer; Tundish; Liquid steel; Buoyancy forces; Inclusions; PIV

1. Introduction

Thermal stratification in convective-stratified flows is usually observed in ladles and tundishes for continuous casting of steel due to the heat loses through their walls, bottom and bath surfaces. Then steel that is fed into the tundish originates a thermally stratified flow that is also influenced by inertial and gravity forces during the passage of steel from the ladle shroud to the tundish outlet. Moreover, fluid flow of steel inside the tundish affects steel quality because non-metallic inclusions should be floated to the bath surface in order to be absorbed by a suitable flux at the melt–flux interface. Steel quality is also affected by the turbulence in the inlet box because the recirculating flow formed, after impacting the tundish bottom; shears the melt–flux interface and entrain flux particles that impair steel cleanliness. Moreover, the melt surface free of flux reacts with nitrogen and oxygen, from the air, provoking reoxidation of steel and affecting its mechanical properties. Actually this kind of flows involve mixed convection because inertial and buoyancy forces play important influences on fluid flow.

Many authors, for example, Miki and Thomas [1] have studied mixed flow convection and it effects on inclusions removal in a tundish taking into account mixed convection effects. Barron et al. [2] studied the effects of mixed convection flow in a tundish heated by a plasma torch using water modeling and mathematical simulation approaches and found considerable changes of the flow pattern when the fluid was heated up. Lopez et al. [3] numerically studied the combined effects of flow control devices and mixed convection and defined the buoyancy number, $Bu = Re/Gr^2$, as the main parameter to quantify the ratio between inertial and buoyancy driven forces. Mathematical simulations of the effects of a varying ladle stream temperature, heat loses and flow control devices on liquid steel flow patterns are reported by Morales et al. [4,5] and Palafox et al. [6]. Thermal

* Corresponding author.
E-mail addresses: rmorales@ipn.mx (R.D. Morales), mdiaz-c@ipn.mx (M. Díaz-Cruz).

0017-9310/03/$ - see front matter
doi:10.1016/S0017-9310(03)00068-1

Nomenclature

Bu	buoyancy number
C	concentration of tracer
C_p	heat capacity
D_{nozzle}	diameter of the nozzle
D_{eff}	effective diffusivity
F_{D}	drag coefficient
h	enthalpy
g	gravity constant
G	viscous dissipation stress tensor
k	kinetic energy
k_{eff}	effective thermal conductivity of fluid
L	bath depth
P	pressure
Pr	Prandtl number
s	particle trajectory length
u	fluid velocity
T	temperature
t	time
v	average fluid velocity through the vessel

Greek symbols

β	thermal expansion coefficient
ϵ	dissipation rate of the kinetic energy
μ	fluid viscosity
θ	dimensionless time
Θ	dimensionless temperature
ρ	density
τ	strain stress tensor
ζ	random number in the random walk mode

disturbs are rapidly detected by the system when hot or cold steel is incoming and found considerable changes of the flow structure when the ratio Gr/Re^2 increases above five.

The purpose of the present study is to complement what has been published regarding mixed convection in continuous casting tundishes by addressing the capacity of mathematical models to predict thermally stratified flows by comparing predicted flow fields with experimental measurements. Other objective is the quantification of the dynamics of buoyancy driven forces activated by inputs of hot fluid and their influence on inclusions flotation.

2. Experimentation

Using the Froude [7] criterion a 2/5 scale plastic model, 2 cm thick, of a one-strand slab tundish of a Brazilian caster was built. The geometric dimensions of this model are shown in Fig. 1(a), the model operates with a slope of 2° with respect of the horizontal plane and has a halved dam as is seen in Fig. 1(b). Due to that inclination the liquid level is slightly higher at the end wall than at the sidewall of the pouring box. A turbulence inhibitor was placed on the tundish bottom, just below the tip of the ladle shroud (LS), in order to obtain a flow closer to the plug pattern. Fig. 2 shows an exploited view of this inhibitor. This device was designed on previous experimental trials in order to provide to the flow the highest volume fraction of the fluid under a plug pattern, which is suitable for floating inclusions [8]. Thermal experiments were performed using hot water step inputs coming from a boiler and introduced into the tundish as a step input signal. Six thermocouples were placed at the axial-symmetrical longitudinal plane of this tundish at different heights as is indicated in Fig. 1(a). Thermocouple 1 was located just in the tip of the LS, point 1, to detect the time of the first signal. Thermocouples 2 and 3 where placed just before the halved dam, point 2, close to the tundish bottom and point 3 close to the bath surface, both temperatures are expected to be different. The other thermocouples 4, 5 and 6 were placed after the halved dam at the same height of thermocouple 2 (point 4), close to the upper corner of the tundish (point 5) and in the outlet (point 6), respectively. These thermocouples were calibrated using a 25 ohm-temperature calibrator Model F-162-CE of Automatic Systems to an accuracy of 0.1 °C. The emf (electromotive force) signals of these thermocouples are digitalized by an interface and are sent to a PC equipped with an acquisition card and software that permits real time recording-plotting procedures of temperature–time curves.

Mass transfer was simulated by means of a pulse injection of 20 cm^3 of red dye solution taken from a 35 g/l original solution. The injection was performed in the ladle shroud and the response of this signal, or tracer concentrations, was continuously monitored in the tundish outlet by pumping the sample into a cell of a spectrophotometer. The records of the tracer concentration were stored in a PC equipped with an acquisition card allowing the plotting of results in a real time. These experiments were carried out under isothermal and non-isothermal conditions. This tundish operates, normally, with a steel flow rate of 3.12 tons/min, which is equivalent to 45 l of water/min according to Froude's criterion [7]. Temperature differences (with respect of the initial water temperatures) varied between 13 and 14 °C.

Fluid flow structure was also monitored using a PIV equipment from Dantec Systems. A green frequency double-pulsed Nd:YAG laser with a wavelength of 532 nm was employed. In order to obtain short bursts of

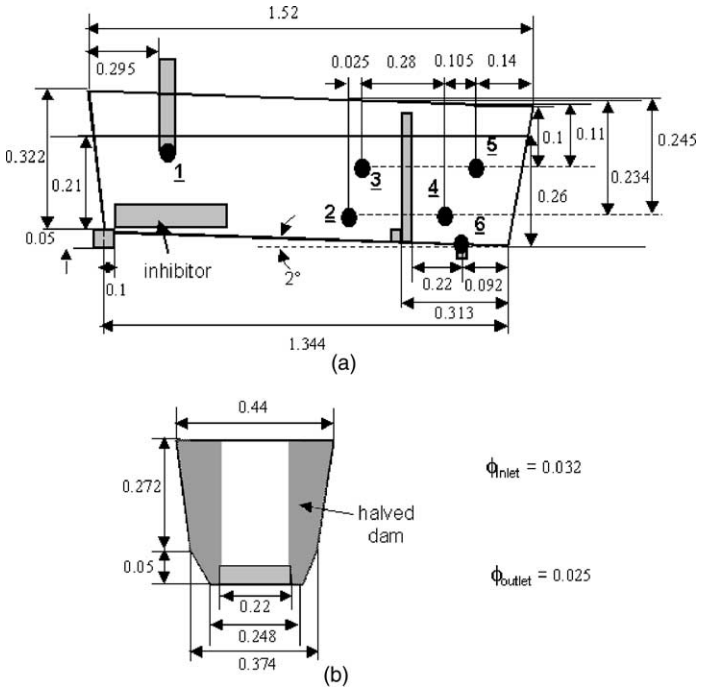

Fig. 1. The geometric dimensions of the tundish (m): (a) longitudinal section, (b) cross section and details of the halved dam.

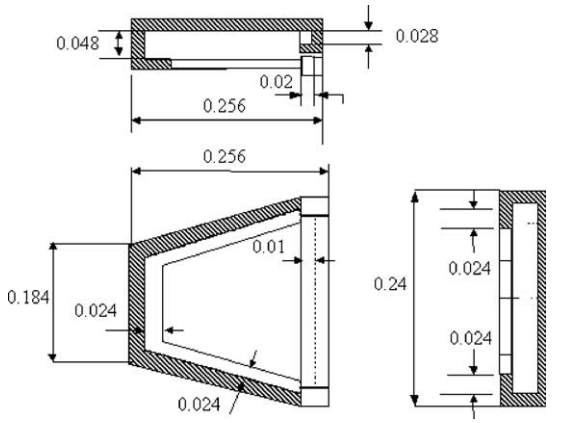

Fig. 2. The geometric dimensions of the turbulence inhibitor (m).

light energy, the lasing cavity is Q-switched so that the energy is emitted in 6–10 ns bursts opposed to pulses of 250 μs, which is the duration of the exciting lamp in the laser cavity. Output energy from the Nd:YAG laser is 20 mJ. This energy is increased with light guides that can transmit 500 mJ of pulsed radiation with an optical transmission that is greater than 90% at 532 nm. Interrogation areas of 1×1 mm in the flow were scanned with a resolution of 32×32 or 64×64 pixels.

The laser light was positioned at the axial-symmetrical plane of the tundish by means of a computer-controlled positioner with 3-D movements to send a longitudinal laser-sheet located in this plane. In order to follow the fluid flow the fluid was previously seeded with polyamide particles with a density of 1030 kg/m^3. A cross-correlation procedure using fast fourier transforms allowed to process the recorded signals and a Gaussian distribution function was used to determine the location of the maximum of the peak displacement with sub-pixel accuracy. The signals were detected by a Dantec charge coupled device (CCD) with 60 mm Nikon lenses and the recordings were processed using a commercial Flow Map software in a Pentium IV PC in order to obtain the vector velocity fields and other derived parameters.

3. Mathematical model

3.1. Equations

The mathematical model to simulate heat and mass transfer in convective-stratified flows is constituted by the following equations,

Equation of continuity

$$\frac{\partial \rho}{\partial t} + \frac{\partial}{\partial x_j}(\rho u_j) = 0 \tag{1}$$

Momentum equation

$$\frac{\partial}{\partial t}(\rho u_i)+\frac{\partial}{\partial x_j}(\rho u_i u_j)=-\frac{\partial P}{\partial x_i}+\frac{\partial}{\partial x_j}\left[\mu_{\text{eff}}\left(\frac{\partial u_i}{\partial u_j}+\frac{\partial u_j}{\partial x_i}\right)\right]+\rho_{\text{ref}}\beta g\,\Delta T \tag{2}$$

the last term involves gravity and buoyancy forces due to thermal stratification and β is the thermal expansion coefficient of water.

Mass transfer equation

$$\frac{\partial C}{\partial t}+u\frac{\partial C}{\partial x}+v\frac{\partial C}{\partial y}+w\frac{\partial C}{\partial z}=D_{\text{eff}}\left(\frac{\partial^2 C}{\partial x^2}+\frac{\partial^2 C}{\partial y^2}+\frac{\partial^2 C}{\partial z^2}\right) \tag{3}$$

Heat transfer equation

$$\frac{\partial}{\partial t}(\rho h)+\frac{\partial}{\partial x_i}(\rho u_i h)=-\frac{\partial}{\partial x_i}\left(k_{\text{eff}}\frac{\partial T}{\partial x_i}\right) \tag{4}$$

where the enthalpy h and the effective thermal conductivity, k_{eff} are controlled mainly by the turbulence level through the turbulent viscosity:

$$k_{\text{eff}}=k_0+\frac{C_p\mu_{\text{t}}}{Pr_t} \tag{5}$$

Equation, which describes the turbulent kinetic energy, according to the k–ϵ model [15], is

$$\frac{\partial}{\partial t}(\rho k)+\frac{\partial}{\partial x_i}\left(\rho u_i k-\frac{\mu_{\text{eff}}}{\sigma_k}\frac{\partial k}{\partial x_i}\right)=G-\rho\varepsilon \tag{6}$$

Equation that describes the dissipation rate of turbulence energy in this model is,

$$\frac{\partial}{\partial t}(\rho\varepsilon)+\frac{\partial}{\partial x_i}\left(\rho u_i\varepsilon-\frac{\mu_{\text{eff}}}{\sigma_\varepsilon}\frac{\partial k}{\partial x_i}\right)=\frac{1}{k}(C_1G-C_2\rho\varepsilon^2) \tag{7}$$

where

$$G=\mu_{\text{t}}\frac{\partial u_i}{\partial x_i}\left(\frac{\partial u_i}{\partial x_i}+\frac{\partial u_i}{\partial x_j}\right) \tag{8}$$

Effective viscosity is the sum of laminar viscosity and turbulent viscosity:

$$\mu_{\text{eff}}=\mu_{\text{l}}+\mu_{\text{t}} \tag{9}$$

Turbulent viscosity is related to the turbulent energy and dissipation rate of turbulent energy by

$$\mu_{\text{t}}=C_{\text{D}}\rho k^2/\varepsilon \tag{10}$$

The values for the constants in this k–ϵ model C_1, C_2, C_{D}, σ_k and σ_ϵ are 1.43, 1.92, 0.09, 1.00 and 1.30, respectively; these values were taken from Launder and Spalding [9].

In the mass transfer equations D_{eff} is the effective mass transfer diffusivity, which is the summation of molecular and turbulent diffusivities, respectively. The effective diffusivity D_{eff} is related to the turbulent viscosity μ_{t} by;

$$D_{\text{eff}}=D_0+\frac{\mu_{\text{t}}}{\rho Sc_t} \tag{11}$$

where D_0 is the molecular diffusivity of a tracer. Since turbulent flow generally carries mass over an equivalent Prandtl mixing length this coefficient was assumed equal to one. The physical properties of water used in this model are; viscosity 0.001 Pa s, density $\rho=654.619+2.5446T-0.004683T^2(K)$, $C_p=4182$ $(\text{J kg}^{-1}\,\text{K}^{-1})$ and $k=0.597$ $(\text{W m}^{-1}\,\text{K}^{-1})$.

3.2. Boundary conditions

No-slip conditions were applied as boundary conditions to all solid surfaces of the tundish including the exterior and interior walls of the inhibitor. Near any solid surface, there is a very thin laminar sublayer. Between the laminar sublayer and the turbulent core, there is also a buffer sublayer, which is in a state between laminar and turbulent flow. Consequently, for nodes near a solid wall, the so-called wall functions are required to calculate the values of a variable since in those places very steep gradients of fluid flow variables occur. If a node in the 3D domain is in the laminar sublayer, a linear relationship between the wall stress and the velocity gradient is assumed

$$\tau_{\text{w}}=\mu\frac{\Delta v}{\Delta n} \tag{12}$$

If the node is beyond the laminar sublayer, the logarithmic law is applied in order to calculate the wall shear stress:

$$\frac{v_p}{v^*}=\frac{1}{\kappa_v}\ln(Ey^+) \tag{13}$$

where

$$v^*=\sqrt{\frac{\tau_{\text{w}}}{\rho}} \tag{14}$$

and

$$y^+=\rho v^*\Delta n_p/\mu \tag{15}$$

κ_v is the Von Karmanás constant (0.42) E is an empirical constant (9.81) taken from reference [10] and v_p is the velocity of the fluid near the wall. Another equation for y^+ is,

$$y^+=\frac{\rho k_p^{1/2}C_\mu^{1/4}\Delta n_p}{\mu} \tag{16}$$

where k_p is the turbulent kinetic energy at the near-wall grid point p and Δn_p is the distance of point p to the wall. Eq. (16) is an empirical fit of turbulent flow data for y^+ between values of 10 and 20. In this study, Eq. (15) is used when y^+ is smaller than 12, and Eq. (16) is used when y^+ is larger than this value. On the top free surface

of the bath and in symmetry planes the fluxes of momentum and mass, as well as the gradients of the turbulent kinetic energy and the dissipation rate of kinetic energy, were all set equal to zero. At the entry jet the flow profile was assumed to be flat and calculated by

$$U_{\text{in}} = Q/A_{\text{nozzle}} \tag{17}$$

The inlet values for k and ϵ at the inlet were calculated with the following equations:

$$k_{\text{in}} = 0.01U_{\text{in}}^2 \tag{18}$$

$$\varepsilon_{\text{in}} = 2k_{\text{in}}^{3/2}/D_{\text{nozzle}} \tag{19}$$

Thermal conditions involve the assumption of negligible heat loses through the wall and bottom of the tundish as well as through the bath surface. That is the system is assumed to be adiabatic as is explained in reference [11]. This assumption is reasonable because energy loses by radiation are very small due to the low temperatures involved and the energy transported by convection is considerably higher that the energy lost through the tundish walls and its bottom.

3.3. Initial conditions

Eqs. (1, (2), (3), (4), (6) and (7) are solved simultaneously together with their boundary conditions, using the auxiliary expressions explained above, until reaching the steady state of the fluid flow. The velocity field calculated was then employed to solve Eq. (3) for the tracer concentration under unsteady state conditions. Here, it is implicitly assumed that the presence of the tracer does not affect the water density in an appreciable extent. The initial condition to solve Eq. (3) is stated as follows:

$$\text{at } t = 0 \quad \text{and} \quad x_0, y_0, z_0 \qquad C = \frac{M}{V_{\text{nozzle}}} \tag{20}$$

where M is the total mass of the tracer and V is the volume of the water column in the ladle shroud from the injection point to the shroud tip assuming a perfect mixing. x_0, y_0 and z_0 are the coordinates of the nozzle tip in the 3D domain. Initial condition for the thermal field is that which considers a uniform temperature throughout the fluid volume at a time just before zero. At time zero an input of well-mixed water at different temperature is introduced in the system and can be mathematically expressed very similarly to Eq. (20),

$$\text{at } t = 0 \quad \text{and} \quad x_0, y_0, z_0 \qquad T = T_{\text{input}} \tag{21}$$

3.4. Numerical solution

The continuity equation, the momentum and mass transfer equations; the initial and all boundary conditions were rewritten in a finite difference scheme. A dense mesh was employed near the tundish bottom and near the tundish walls just to avoid inconsistencies when the wall function is applied as a boundary condition. A dense mesh was also employed in the outlet-longitudinal planes as well as in the proximity of the stopper rods. The numerical algorithm used to solve those equations is known as SIMPLE [12]. The total numbers of cells in this 3D domain counted 80 000. A criterion for convergence in all cases simulated here was established when the sum of all residuals for the variables was less than 10^{-6}. Velocity fields at steady state were first calculated and later they were employed to solve the mass transfer equation. The mathematical model was run in a workstation silicon graphics model O2 with R 10 000 processors at the Laboratory for Simulation of Materials Processing of IPN-ESIQIE, Department of Metallurgy and Materials Engineering. The computer results were stored in CDás to be arranged in a special format, for further analysis, by feeding them into commercial plotting software known as Tecplot.

3.5. Trajectory of inclusions

Inclusion trajectories were calculated using a Lagrangian particle tracking approach [13], which solves a transport equation for each inclusion as it travels through the previously calculated flow field of water. The mean local-inclusion velocity components ($\bar{u}_i$) needed to obtain the particle path are calculated from the following balance, which includes the drag and buoyancy forces relative to water;

$$\frac{\mathrm{d}\bar{u}_i}{\mathrm{d}t} = F_{\text{D}}(u_i - \bar{u}_i) + \frac{\rho_i - \rho_q}{\rho_i} g_j \tag{22}$$

where F_{D} is the drag coefficient and is a function of the Reynolds number. To simulate the chaotic effect of the turbulence eddies on the inclusion trajectories, a discrete random-walk model was applied [13]. In this model, a fluctuant random-velocity vector (u_i') is added to the calculated time-averaged vector ($\bar{u}_i$) in order to obtain the inclusion velocity (u_i) at each time step as "i" travels through the fluid. Each random component of the inclusion velocity is proportional to the local turbulent kinetic energy level, according to the following Equation:

$$u_i' = \zeta_i \sqrt{\bar{u}_i'^2} = \zeta_i \sqrt{\frac{2k_p}{3}} \tag{23}$$

where ζ_i is a random number, normally distributed between -1 and 1, which changes at each integration step and k_p is the kinetic energy at node p. Once knowing the fluid velocity fields and the velocity of inclusions their trajectories were calculated through their integration with time,

$$s = \int_0^t \bar{u}_i \, dt \tag{24}$$

Boundary conditions of totally elastic impact of particles on all solid surfaces were assumed. Although this is a non-realistic assumption this was done so to emphasize the effects of buoyancy forces on the trajectories of solid particles in the flow.

4. Results and discussion

4.1. Isothermal experiments

Fig. 3(a)–(c) show the isothermal fluid flow structures of water in the model determined through PIV and Fig. 3(d) shows the results of mathematical simulations, respectively. Agreement between both types of data is very good and, as seen, the flow follows very closely a plug pattern, which indicates that the inhibitor and the geometry of this vessel yield good flow characteristics for floating inclusions. In the pouring box, the inhibitor neutralizes outward fluid velocities; at the central part of the vessel the flow is oriented toward the outlet along the symmetry plane and the same happens at the outlet box where a small recirculating flow is observed and it is formed by the fluid that impacts the end-wall of this tundish.

Mass transfer experiments recorded in a video image are reported in Fig. 4(a), 60 s after the tracer injection. At this time dispersion of the tracer reaches zones that are close to the pouring box and the fluid that is driven by the momentum imparted by the impact with the inhibitor, has the highest concentrations as in indicated by the blackest zone. These results should be compared with the mathematical simulations presented in Fig. 4(b) where the magnitudes of the concentration contours, in mass fraction percent agree very well with the intensity of colors shown in Fig. 4(a). This indicates the excellent capacity of the mathematical simulations to predict momentum and mass transfer in this system. Fig. 4(c)–(d) show simulation results for times 120, and 240 s after the injection of the tracer. As is seen flow dispersion follows a plug flow pattern corresponding to the velocity fields shown in Fig. 3(a)–(d). Mass transfer results were plotted using dimensionless concentration and time variables defined by (see nomenclature of symbols),

$$C = C_i/(M/Q) \tag{25}$$

$$\theta = t/\bar{t} \tag{26}$$

where the mean residence time is given by,

$$\bar{t} = \frac{\sum C_i t_i}{\sum C_i} \tag{27}$$

This plot is shown in Fig. 5a for the experimental results obtained through the recordings of the spectrophotometer and for the mathematical simulations obtained form the computer files. This comparison demonstrates the usefulness of mathematical simulations to describe mass transfer phenomena under isothermal conditions. One point to be noticed is the long minimum residence time of the tracer inside the vessel whose magnitude is directly related with the volume fraction of fluid that obeys the plug flow. Using statistical methods, that are well known in chemical engineering field [14,15], the volume fractions of fluid under plug flow, back mixing flow and dead non-interactive volume were calculated

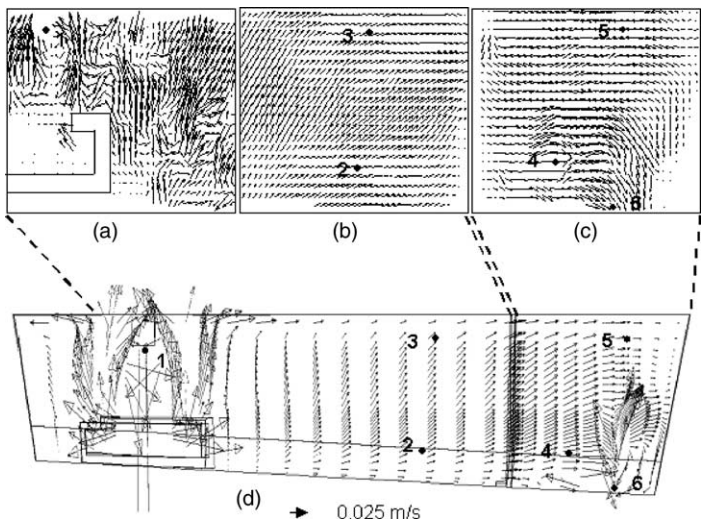

Fig. 3. Velocity fields of water under isothermal conditions: (a)–(c) experimental measurements with PIV, (d) mathematical simulations.

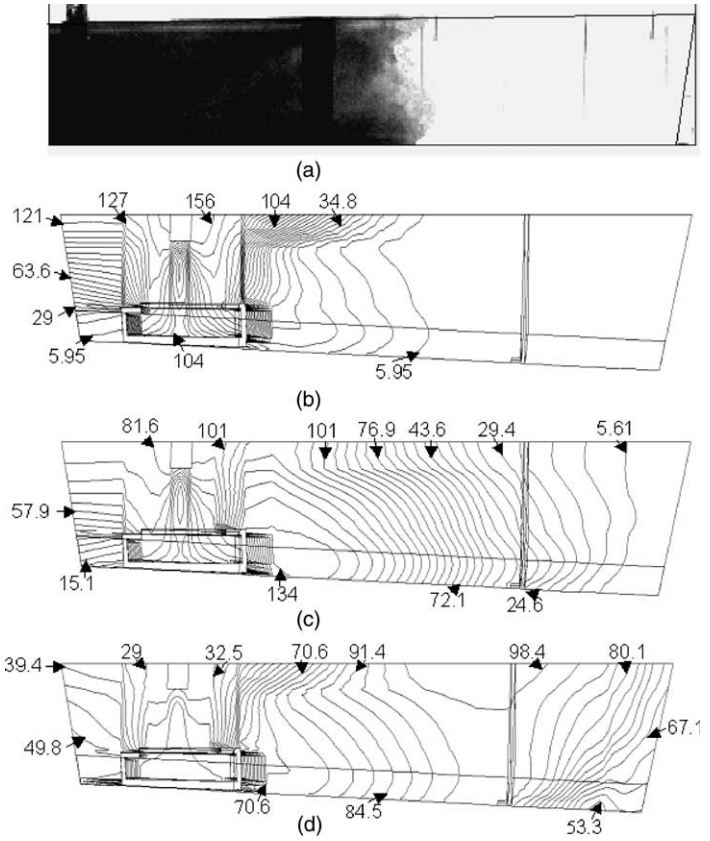

Fig. 4. Concentrations contours in mass % $\times 10^{-4}$ under isothermal conditions: (a) video image of the tracer dispersion in the flow 60 s after its injection, (b)–(d) mathematical simulations of tracer dispersion in the flow 60, 120 and 240 s after the injection of the tracer, respectively.

from the residence time distribution (RTD) curve using the following relationships:

$$\frac{V_p}{V} = \theta_{min} \tag{28}$$

where V_p is the fluid volume that follows a plug flow pattern, V is the total fluid volume n the vessel and θ_{min} is the minimum dimensionless time in Fig. 5. In practical terms all fluid remaining at dimensionless times θ greater than 2.0 can be regarded as dead volume.

$$\frac{V_d}{V} = 1 - \theta\frac{Q}{V} \tag{29}$$

and the mixed fraction will be,

$$\frac{V}{V_m} = 1 - \left(\frac{V_p}{V} + \frac{V_d}{V}\right) \tag{30}$$

From curve in Fig. 5(a) and the precedent expressions the results obtained for the plug flow fractions are 43.65%, 54.15% and 2.20%, respectively. Indeed, this volume fraction with a plug flow pattern is the highest among all other published results for any kind of tundish design [4–6,8,16,17] and this is in agreement with the experimental flow measurements made with the PIV and with the mathematical simulations.

4.2. Non-isothermal experiments

Fig. 6(a) and (b) show the corresponding flow structures measured with the PIV while Fig. 6(c) shows the mathematical simulations 90 s after the step input of hot water. At this time the flow is clearly stratified as is seen by the presence of a counter flow close to the tundish bottom forming a well-defined recirculating flow before the halved dam. Here the liquid velocity is highest close to the bath surface transporting fluid directly to the outlet box thanks to the buoyancy forces that are working together with the inertial ones. This flow, ushered by mixed convection mechanisms, impacts the end wall forming a recirculating flow in the outlet box. A general agreement between measured vector fields and calculated ones can be seen in Fig. 6(a)–(c). As the time increases temperature gradients and buoyancy forces decrease and the fluid flow will resemble more that

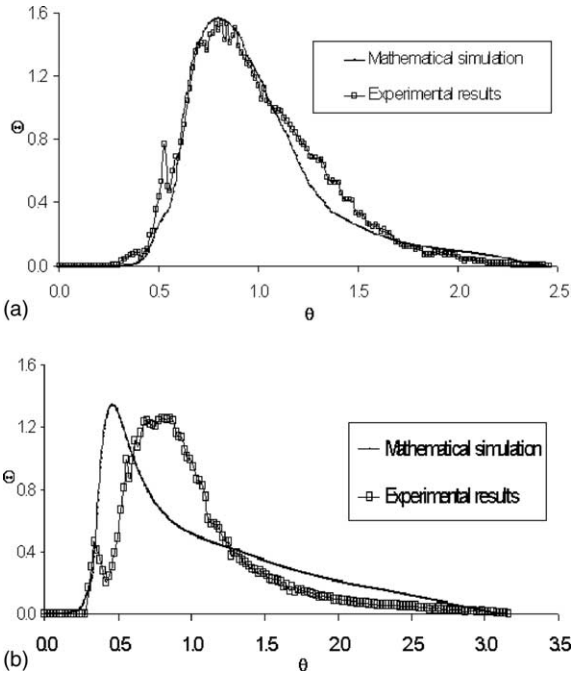

Fig. 5. Experimental and simulated residence time distribution curves: (a) isothermal conditions, (b) non-isothermal conditions.

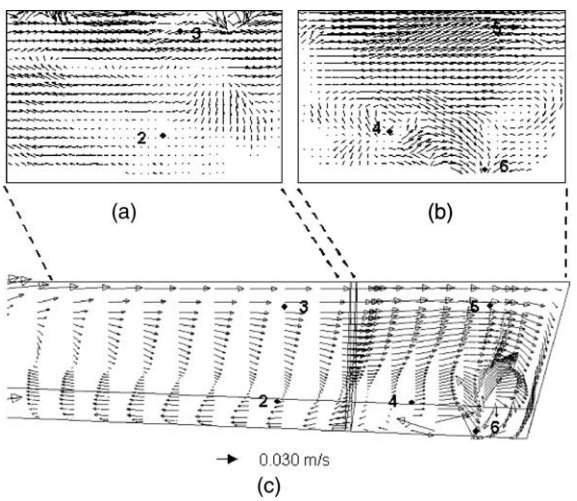

Fig. 6. Velocity fields of water under non-isothermal conditions: (a, b) PIV measurements after 90 s of the hot water step input, (c) Mathematical simulations after 90 s of the hot step input.

corresponding to the isothermal conditions shown in Fig. 3(a)–(d).

Temperature recordings were plotted using a dimensionless temperature defined by,

$$\Theta = \frac{T - T_i}{T_f - T_i} \tag{31}$$

where T is the current recorded temperature at given node or point, T_i is the initial bath temperature and T_f is the step temperature or the temperature at very long times when a new steady-isothermal state has been attained. The dimensionless time is defined as in Eq. (25) but the mean residence time is referred here to the residence time of the thermal signal, which is similar to Eq. (26) using temperature recordings instead of concentrations;

$$\bar{t} = \frac{\sum T_i t_i}{\sum T_i} \tag{32}$$

Fig. 7 shows a plot of Θ vs θ for every point of temperature measurement as was described in the description of experiments. The hot water step input is almost perfect as is seen in Fig. 7 and the differences of temperature among the measurement points provide a quantitative idea about the temperature gradients generated inside the vessel. In this Fig. 7 the mathematical prediction for the outlet temperature is also plotted and it can be compared with the corresponding experimental measurements at the tundish outlet. As is seen the mathematical simulations over predicts slightly the experimental outlet temperature probably due to the influence of the adiabatic conditions assumed in the model when the heat fluxes through the wall and bottom of the tundish and the bat surface were set equal to zero.

One of the frequent questions that arise during the operation of tundishes is what is the magnitude of the buoyancy forces imposed by changes of temperature of the entering stream since these forces may influence the flotation of inclusions. In order to estimate these buoyancy forces the following procedure was applied:

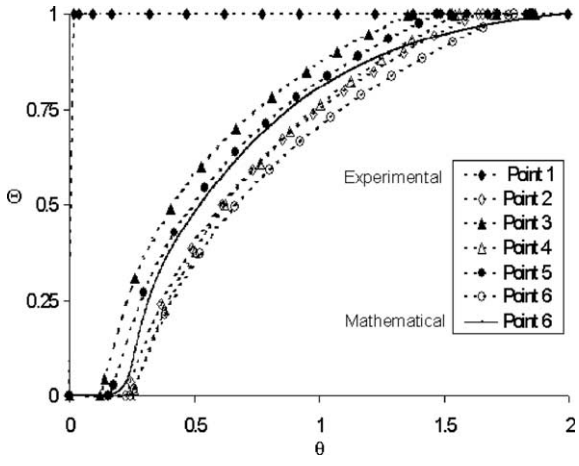

Fig. 7. Thermal behavior of water under the influence of a hot water step input.

First we can express the temperature difference between the step temperature and any point inside the tundish as a function of the thermal RTD curve in Fig. 7 as follows:

$$\Delta T = (1-\Theta)T_f + (\Theta - 1)T_i \tag{33}$$

Using this temperature difference is possible to evaluate the buoyancy number, $Bu = Gr/Re^2$ as a function of the thermal RTD curve as seen in the following Eq. (34)

$$Bu = \frac{g\beta L}{v^2}[(1-\Theta)T_f + (\Theta - 1)T_i] \tag{34}$$

where, L is a characteristic length of the system (usually the bath height), β the thermal expansion coefficient of water, 2.95×10^{-4} K^{-1}, g is the gravity constant and v is the average water velocity through the cross section of the tundish. Moreover, the derivation of Eq. (34) with respect of the dimensionless time can be useful to evaluate the change rate of the ratio between the buoyancy forces and inertial forces, due to changes of fluid density promoted by thermal gradients,

$$\frac{d(Bu)}{d\theta} = \frac{g\beta L}{v^2}(T_i - T_f)\frac{d\Theta}{d\theta} \tag{35}$$

Thus the variations of the buoyancy number, in a given location inside the tundish can be obtained through a simple derivation of the Θ curves of Fig. 7 obtained from the thermal experiments, and substituting this derivative in Eq. (35).

On the other hand, buoyancy forces on the fluid volume promoted by thermal gradients in the tundish are defined as,

$$F_b = \rho_{ref}\beta\Delta T g_i \tag{36}$$

where ρ_{ref} is a reference density for water like 1000 kg/m^3. Substitution of Eq. (33) in Eq. (36), applying the derivation of the resultant expression with respects the dimensionless time and using the result expressed in Eq. (35) we find;

$$\frac{dF_b}{d\theta} = \rho_{ref} g\beta(T_i - T_f)\frac{d\Theta}{d\theta} \tag{37}$$

Thus Eq. (37) provides us the rate change of the buoyancy force per unite volume of fluid through the derivative of the "thermal RTD" curve, Θ, the results are shown in Fig. 8. Points 3 and 5 report the largest buoyancy forces, thus in these regions of the tundish buoyancy forces would compete with the inertial ones acting downstream. Consequently with this discussion being buoyancy forces large this would be useful to enhance the flotation rate of inclusions. However, it is also true that unfortunately this transient is very short and its enhancing effect lasts only during a very short period. Buoyancy forces in points 2, 4 and 6 maintain similar behaviors.

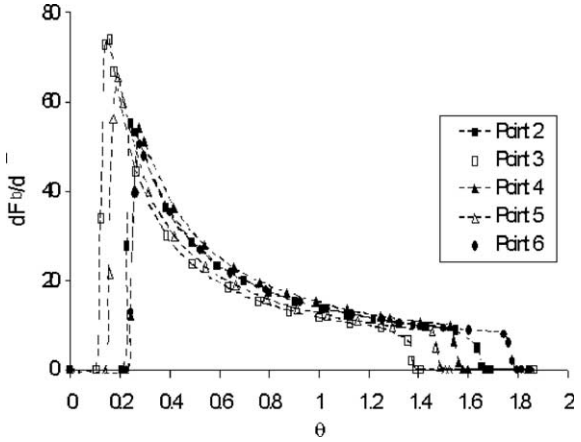

Fig. 8. Estimated bouyancy forces per unit volume in water under non-isothermal conditions.

Mass transfer is also very affected by the existence of these buoyancy forces as can be seen in Fig. 9(a)–(c). Fig. 9(a) shows the mathematical simulation of the tracer dispersion 60 s after the pulse injection, this figure should be compared with Fig. 4(b). Buoyancy forces promote a strong recirculating flow with large velocities upstream close to the tundish bottom and large velocities downstream close to the bath surface as is seen in Fig. 6(a) and (b). The tracer concentration fields yield "S" shaped contours along the tundish length as a

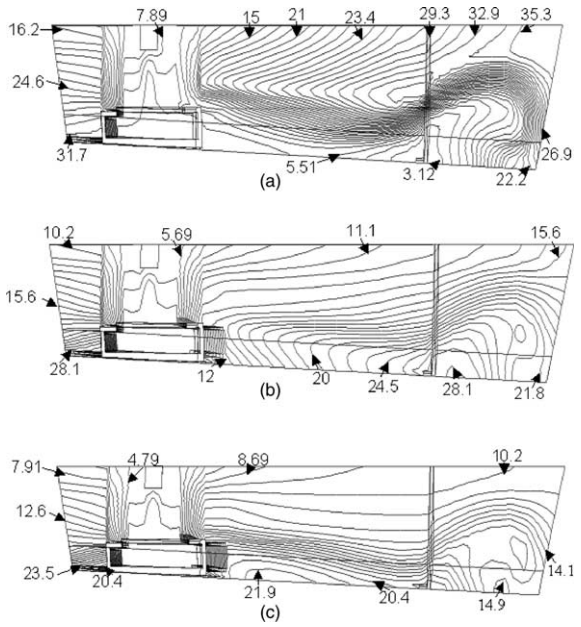

Fig. 9. Concentrations contours in mass % $\times 10^{-4}$ under non-isothermal conditions: (a)–(c) Mathematical simulations of tracer dispersion in the flow 60, 90 and 120 s after the injection of the tracer, respectively.

consequence of this complex flow. Fig. 9(b) and (c) show the concentration contours 90 and 120 s after the pulse injection. The RTD curve of the non-isothermal experiment in terms of dimensionless concentration and dimensionless time is shown in Fig. 5(b) and it reports a shorter residence time originated by the faster fluid flow close to the bath surface, which promotes a faster mass transportation toward the tundish outlet. In this figure there is also shown the calculated curve through the mathematical model and again there is a difference between both type of data originated probably by the assumption of adiabatic conditions in the system.

4.3. Trajectories of inclusions

Smaller inclusions are the most difficult to be floated out consequently, in these simulations, particles with sizes from 1 to 10 μm were assumed. For comparison purposes larger inclusions with sizes from 10 to 50 μm were aslso simulated. Density of these particles was constant and equal to 500 kg/m^3. This is equivalent to the density ratio between alumina inclusions and liquid steel. Using the Lagrangian model inclusion trajectories (1–10 μm) were calculated for the isothermal conditions and the results are shown in Fig. 10(a). Inclusion trajectories for the non-isothermal conditions 90 s after the step input of hot water are shown in Fig. 10(b). Effects of increasing particle sizes between 10 and 50 μm are shown in Fig. 10(c) and (d), respectively for the same fluid flow conditions already described. As is seen, smaller particles, Fig. 10(a), follow trajectories driven, initially, by the inhibitor, toward the bath surface. However, many particles suffer bypassing toward the outlet because they are unable to float out. Under the effects of buoyancy forces these small inclusions flow closer to the bath surface as is seen in Fig. 10(b) and is very important to notice that most of these small inclusions do not touch the bath surface where they may absorbed by a slag. Then the existence of buoyancy forces, even if they are relatively large, as reported in Fig. 8, do no guarantee an efficient flotation of small inclusions. For larger inclusions under isothermal conditions trajectories of inclusions follow irregular "S" shaped trajectories, Fig. 10(c), and under the influence of buoyancy forces their trajectories are straightly directed downstream as is seen in Fig. 10(d). Due to their

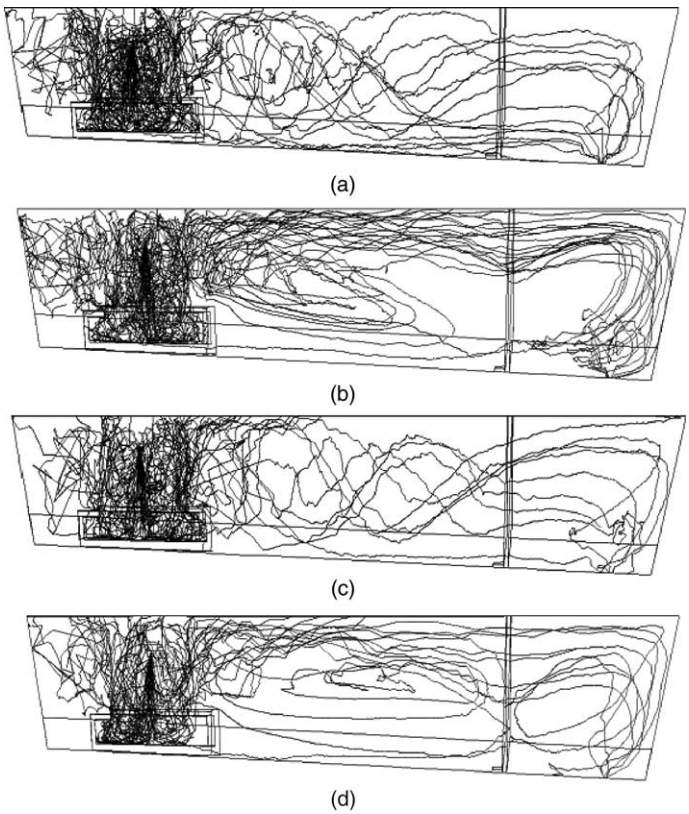

Fig. 10. Trajectories of inclusions in the water flow: (a) isothermal conditions and particle sizes from 1 to 10 μm, (b) non-isothermal and particles sizes from 1 to 10 μm, (c) isothermal conditions and particle sizes from 10 to 50 μm, (d) non-isothermal conditions and particles sizes from 10 to 50 μm.

large sizes these inclusions are prone to float out by the simple effect of the inhibitor and by the buoyancy forces promoted by temperature gradients.

From this discussion it can be stated that buoyancy forces originated by thermal gradients are not enough to enhance the flotation of small inclusions, rather they impair their elimination because of their entrainment by the fluid directly to the outlet. On the other hand, flotation enhancement of larger inclusions by these buoyancy forces is rather small and the beneficial effects of the inhibitor seem to be larger.

5. Conclusions

Steel flow, heat and mass transfer and inclusions trajectories were simulated in a water model using isothermal and non-isothermal conditions. Fluid flow structure was determined through Particle Image Velocimetry techniques and the main conclusions derived from this study are as follows.

(1) Under isothermal conditions fluid flow approaches to an ideal plug flow and mass transfer phenomena yield concentration distributions that follow the same pattern.

(2) Under non-isothermal conditions the fluid flow structure departures from the plug flow and fluid velocities are larger close to the bath surface as a consequence of the presence of buoyancy forces.

(3) Large fluid velocities near the bath surface increase a by pass flow carrying tracer from the inlet directly to the outlet along the bath surface. Consequently, the minimum residence time of tracer inside the vessel becomes smaller.

(4) As a consequence of the precedent conclusion small inclusions are entrained by the buoyancy-driven downstream flow promoting bypass transportation toward the outlet. Flotation of large inclusions are slightly enhanced by thermal buoyancy forces and the influence of flow control devices such as the inhibitor play a more important role to eliminate them.

(5) Design of flow control devices to eliminate inclusions is more important than the magnitude of thermally driven buoyancy forces. Agglomeration of small inclusions inside the inhibitor to become into larger ones would be more important for their elimination.

Acknowledgements

The authors are very acknowledged to CoNaCyT for the financial support to this work. Thanks are also given to the institutions SNI and IPN for their permanent support to the activities of the Simulation of Materials Processing and Fluid Dynamics Group.

References

[1] Y. Miki, B.G. Thomas, Modeling of inclusion removal in a tundis, Metall. Mater. Trans. 30B (1999) 639–654.
[2] M.A. Barron-Meza, J. de J Barreto-Sandoval, R.D. Morales, Physical and mathematical models of steel flow and heat transfer in a tundish heated by plasma, Metall. Mater. Trans. 31B (2000) 63–74.
[3] S. Lopez-Ramirez, R.D. Morales, A. Serrano, Numerical simulation of the effects of buoyancy forces and flow control devices on fluid flow and heat transfer of liquid steel in a tundish, Numer. Trans. 37 (2000) 63–74.
[4] R.D. Morales, S. López-Ramírez, J. Palafox-Ramos, D. Zacharias, Mathematical simulation of effects of flow control devices and buoyancy forces on molten steel flow and evolution of output temperatures, Ironmak. steel mak. 28 (1) (2001) 33–43.
[5] R.D. Morales, J. de J Barreto, S. López-Ramírez, J. Palafox-ramos, M. Díaz-Cruz, Mathematical simulation of the influence of buoyancy forces on the molten steel flow in a continuous casting tundish, Model. Simul. Mater. Sci. Eng. 8 (2000) 781–801.
[6] J. Palafox-Ramos, J. de J Barreto-S, S. López-Ramírez, R.D. Morales, Melt flow optimization using turbulence inhibitors in large volume tundishes, Ironmak. Steelmak. 28 (2) (2001) 101–109.
[7] L.J. Heaslip, A. McLean, I.D. Sommerville, in: Continuous Casting, vol. 1, iron and steel Society, Warrendale, PA, 1983, pp. 99–112.
[8] S. López-Ramírez, J. de J Barreto-S, J. Palafox-Ramos, R.D. Morales, D. Zacharias, Modeling study of the influence of turbulence inhibitors on molten steel flow, tracer dispersion and inclusion trajectories in tundishes, Metall. Mater. Trans. 32B (2001) 615–627.
[9] B.E. Launder, D.B. Spalding, The numerical computation of turbulent flows, Comput. Methods Appl. Mech. Eng. 3 (1974) 269–289.
[10] J. de J Barreto-Sandoval, M.A. Barron-Meza, R.D. Morales, Physical and mathematical modeling of steel flow and heat transfer in tundishes under no-isothermal conditions, Iron Steel Inst. Jpn Int. 36 (1996) 543–552.
[11] D.A. Anderson, Computational fluid mechanics and heat transfer, Mc-Graw-Hill Books Co., New York, Mexico City.
[12] S.V. Pantakar, Numerical heat transfer and fluid flow, Hemisphere Publishing Co, Washington, London, 1980.
[13] C. Crowe, M. Sommerfeld, Y. Tsuji, Multiphase flows with droplets and particles, CRC Press, New York, London, 1998.
[14] O. Levenspiel, Chemical reaction engineering, Wiles & Sons, New York, Toronto, 1999.
[15] H.S. Fogler, Elements of chemical reaction engineering, Prentice Hall, London, 1992.
[16] S. Singh, S.C. Koria, Model study of flow of steel in the tundish, ISIJ Int. 33 (1993) 1228–1237.
[17] S. Singh, S.C. Koria, Study of fluid flow in tundishes due to different types of inlet streams, Steel Res. 66 (1995) 294–300.